J. Fluid Mech. (2014), *vol.* 752, *pp.* 39–65.
doi:10.1017/jfm.2014.320

Numerical simulations of self-propelled jumping upon drop coalescence on non-wetting surfaces

Fangjie Liu[1], Giovanni Ghigliotti[2,‡], James J. Feng[2,3,†] and Chuan-Hua Chen[1,†]

[1]Department of Mechanical Engineering and Materials Science, Duke University, Durham, NC 27708, USA

[2]Department of Mathematics, University of British Columbia, Vancouver, BC, Canada V6T 1Z2

[3]Department of Chemical and Biological Engineering, University of British Columbia, Vancouver, BC, Canada V6T 1Z3

(Received 7 October 2013; revised 28 May 2014; accepted 31 May 2014; first published online 2 July 2014)

Coalescing drops spontaneously jump out of plane on a variety of biological and synthetic superhydrophobic surfaces, with potential applications ranging from self-cleaning materials to self-sustained condensers. To investigate the mechanism of self-propelled jumping, we report three-dimensional phase-field simulations of two identical spherical drops coalescing on a flat surface with a contact angle of 180°. The numerical simulations capture the spontaneous jumping process, which follows the capillary–inertial scaling. The out-of-plane directionality is shown to result from the counter-action of the substrate to the impingement of the liquid bridge between the coalescing drops. A viscous cutoff to the capillary–inertial velocity scaling is identified when the Ohnesorge number of the initial drops is around 0.1, but the corresponding viscous cutoff radius is too small to be tested experimentally. Compared to experiments on both superhydrophobic and Leidenfrost surfaces, our simulations accurately predict the nearly constant jumping velocity of around 0.2 when scaled by the capillary–inertial velocity. By comparing the simulated drop coalescence processes with and without the substrate, we attribute this low non-dimensional velocity to the substrate intercepting only a small fraction of the expanding liquid bridge.

Key words: breakup/coalescence, computational methods, drops and bubbles

1. Introduction

When two drops coalesce on a superhydrophobic surface (figure 1), the merged drop self-propels itself to jump perpendicular to the surface (Boreyko & Chen 2009). The self-propelled jumping has been reported on a variety of natural water-repellent surfaces, including those on springtails, lacewings and cicadas (Helbig *et al.* 2011; Watson *et al.* 2011; Wisdom *et al.* 2013). For engineering applications, the jumping motion has been applied to develop superhydrophobic surfaces that are anti-dew

†Email addresses for correspondence: jfeng@math.ubc.ca, chuanhua.chen@duke.edu

‡Present address: Laboratoire de Physique de la Matière Condensée, CNRS UMR 7336, Université de Nice Sophia-Antipolis, Parc Valrose, 06108 Nice CEDEX 2, France.

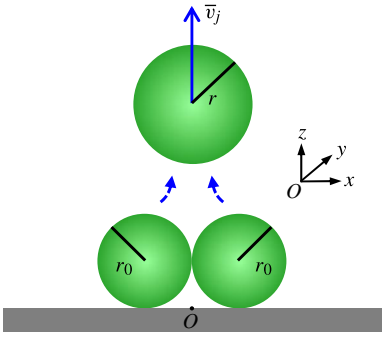

FIGURE 1. (Colour online) Schematic of the drop coalescence process on a non-wetting substrate. Two adjacent drops with an initial radius r_0 coalesce into a larger spherical drop with an equilibrium radius of $r = 2^{1/3}r_0$. The reduction in surface area releases excess surface energy, powering the merged drop to jump away from the substrate. In the coordinate system adopted here, the origin O is attached to the non-wetting surface, the drop coalescence is along the x direction, and the mass-averaged jumping velocity ($\bar{v}_j$) of the merged drop is along the z axis.

(Boreyko & Chen 2009; Enright *et al.* 2012; Feng *et al.* 2012; Rykaczewski *et al.* 2012*b*), anti-icing (Boreyko & Collier 2013; Zhang *et al.* 2013) or self-cleaning (Wisdom *et al.* 2013), as well as heat transfer systems that enhance dropwise condensation (Chen *et al.* 2007; Dietz *et al.* 2010; Cheng, Vandadi & Chen 2012; He *et al.* 2012; Miljkovic *et al.* 2013) and promote thermal rectification (Boreyko, Zhao & Chen 2011; Boreyko & Chen 2013). Despite considerable interest in the jumping phenomenon, the mechanistic understanding is still very primitive, with only capillary–inertial scaling laws (Kollera & Grigull 1969; Boreyko & Chen 2009). Previous modelling efforts are mostly based on energetic arguments with no detailed account of the flow physics, and an *ad hoc* form of viscous dissipation has often been assumed for the energy balance (Wang, Yang & Zhao 2011; Liu *et al.* 2012; Lv *et al.* 2013; Peng *et al.* 2013; Liu, Cheng & Quan 2014*b*).

The limitations of the capillary–inertial scaling laws can be understood by examining the energetic point of view. When two identical drops of radius r_0 coalesce into a larger one (figure 1), the equilibrium radius is $r = 2^{1/3}r_0$ for the merged drop with a mass of $m = (8/3)\rho_L \pi r_0^3$, where ρ_L is the density of the liquid. The overall surface area is reduced upon coalescence, leading to the release of an amount of surface energy of $\Delta E_s = 4\sigma\pi r_0^2(2 - 2^{2/3})$, where σ is the surface tension of the air–liquid interface. The presence of the substrate breaks the symmetry of energy release and the merged drop eventually jumps up. The symmetric coalescence of two identical drops leads to a vertical jumping velocity ($\bar{v}_j$), which is expected to follow the capillary–inertial scaling,

$$\bar{v}_j \sim u_{ci} = \sqrt{\frac{\sigma}{\rho_L r_0}}, \tag{1.1}$$

where u_{ci} is the capillary–inertial velocity. In fact, if all the released surface energy were converted to kinetic energy, the merged drop could achieve a jumping velocity of $\sqrt{2\Delta E_s/m} = 1.11u_{ci}$. It is interesting to note that the energetic argument recovers the wave velocity for capillary disturbances emanating from the point of coalescence.

The $r_0^{-1/2}$ scaling in (1.1) has indeed been confirmed by the experiments with coalescing drops of water condensate on textured superhydrophobic surfaces (Boreyko & Chen 2009). However, two puzzles remain to be solved. (i) The jumping velocity of the merged drop is significantly smaller than the capillary–inertial velocity, with $\bar{v}_j \approx 0.2u_{ci}$. In terms of the energy conversion efficiency, the kinetic energy associated with the jumping motion is less than 4 % of the total released surface energy ($(1/2)m\bar{v}_j \lesssim 4\,\%\ \Delta E_s$). (ii) On textured superhydrophobic surfaces, the capillary–inertial scaling is no longer observed when the drop radius is below a threshold of around 30 μm. This threshold is well above the viscous length scale of 10 nm based on $Oh \sim 1$, where the Ohnesorge number Oh denotes the relative importance of viscous versus capillary–inertial effects,

$$Oh = \frac{\mu_L}{\sqrt{\rho_L \sigma r_0}}, \tag{1.2}$$

where μ_L is the liquid viscosity. These remaining puzzles on the jumping velocity and cutoff radius are of practical significance, for example, in designing vapour chambers with orientation-independent jumping condensate (Boreyko & Chen 2013) and superhydrophobic condensers with effective condensate removal (Miljkovic & Wang 2013). The recent study by Nam, Kim & Shin (2013) has simulated the interfacial flow associated with the jumping process, but has not addressed these puzzles on the capillary–inertial scaling.

We will investigate the remaining puzzles in this paper by numerical simulations. For simplicity, we simulate two adjacent water drops, surrounded by air, coalescing on a flat substrate with a contact angle of 180°. Theoretically, this idealized superhydrophobic surface helps to eliminate the singularity with moving contact lines (Huh & Scriven 1971; Benilov & Vynnycky 2013). In practice, near-180° contact angles are observed not only with water drops on superhydrophobic surfaces but also with mercury drops on flat surfaces, both leading to self-propelled jumping (Kollera & Grigull 1969; Boreyko & Chen 2009). The perfectly non-wetting case can also be approximated by Leidenfrost surfaces, on which liquid drops float on a vapour layer when the solid surfaces are heated well above the boiling point (Leidenfrost 1756; Quéré 2013); for details see our companion paper (Liu *et al.* 2014*a*).

The jumping motion is a consequence of the non-wetting substrate interfering with the oscillation of the coalesced drop. In this sense, our work is related to prior work on drop coalescence, both unconfined in the air and bounded by the substrate. The merging process in figure 2 resembles that of the 'regime I' coalescence upon drop collision at low Weber numbers in Qian & Law (1997); see also a review by Orme (1997). Neglecting the early-stage bridging process (Eggers, Lister & Stone 1999; Thoroddsen, Takehara & Etoh 2005; Paulsen, Burton & Nagel 2011; Sprittles & Shikhmurzaev 2012), the initial condition in figure 2 can be viewed as a large-amplitude two-lobed perturbation to the merged drop at spherical equilibrium. As such, our work is also related to the nonlinear oscillation of a single drop; see e.g. Trinh & Wang (1982) and Basaran (1992).

In the presence of a substrate, the drop coalescence process is significantly modified by the impermeable wall as well as the adhesion between the sessile drops and the substrate, if any. On a hydrophilic surface, the merged drop spreads without any jumping motion (Andrieu *et al.* 2002; Ristenpart *et al.* 2006; Kapur & Gaskell 2007; Hernández-Sánchez *et al.* 2012; Lee *et al.* 2012). In contrast, on a superhydrophobic surface, a liquid bridge between the coalescing drops forms above the substrate

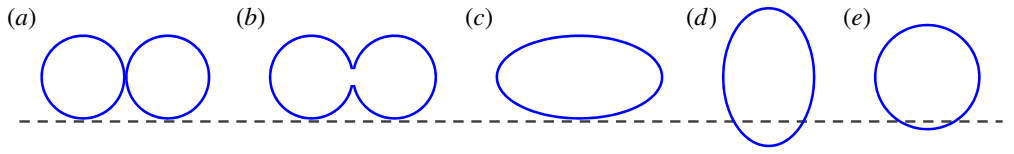

FIGURE 2. (Colour online) The mechanism of jumping can be schematically understood from the coalescence process in the air, without any substrate. (*a*) Two initially distinct drops of identical size are adjacent to each other. (*b*) Upon initiation of coalescence, a liquid bridge is formed to merge the two separate drops into one. (*c*,*d*) The merged drop undergoes many cycles of capillary–inertial oscillations between oblate and prolate shapes. (*e*) The merged drop eventually relaxes to a spherical one due to viscous dissipation. The dashed line indicates the position of an imaginary substrate. Had an impermeable substrate been present at the dashed line as in figure 1, the top-down symmetry of the oscillations would be broken and the merged drop would be forced to move upwards. Note that the actual drop shape is more complex than a spheroid, so oblate and prolate loosely refer to cases with the major axis parallel and perpendicular to the imaginary substrate, respectively.

and the expanding bridge impinges upon it at a later time; upon impingement, the merged drop is forced by the non-wetting substrate first to deform laterally and then to recoil perpendicularly to jump out of plane (Boreyko & Chen 2009, 2010). In fact, on any hydrophobic surface with a contact angle greater than 90°, the liquid bridge initiates at a position above the substrate. However, prior studies of drop coalescence on (super)hydrophobic surfaces typically use drop sizes comparable to or larger than the capillary length (Menchaca-Rocha *et al.* 2001; Nilsson & Rothstein 2011; Mertaniemi *et al.* 2012), and self-propelled jumping has not been observed because of gravitational effects.

In this paper, we will first present a physical model for the self-propelled jumping with phase-field numerical solutions. The numerical results will be compared with experimental data on both superhydrophobic surfaces (Boreyko & Chen 2009) and Leidenfrost surfaces as reported in our companion paper (Liu *et al.* 2014*a*). The physical insights from the numerical simulations will then be used to resolve the aforementioned puzzles.

2. Numerical model

We first develop a numerical model of the coalescence-induced jumping process. The physical assumptions and numerical implementations of the model are discussed.

2.1. *Physical model*

As sketched in figure 1, our physical model consists of two static drops coalescing on a perfectly flat substrate with a contact angle of 180°. Gravity is neglected since the radii of the jumping drops of interest here are much smaller than the capillary length. Within this framework, the jumping motion is a consequence of the interaction between the oscillation of the merged drop and the non-wetting substrate (figure 2).

To understand the jumping mechanism, it is helpful first to review drop coalescence in the air, schematically shown in figure 2. Without any interaction with the substrate, two initially distinct drops will merge by the formation of a liquid bridge. Following the expansion of the liquid bridge, the merged drop will oscillate between oblate

and prolate shapes, eventually relaxing by viscous action to a larger spherical drop. In the absence of the substrate, top-down symmetry is preserved throughout the oscillation process. Note that part of the oscillating drop crosses the imaginary substrate represented by a dashed line, which must be the case because the radius of the merged drop is larger than that of the initial drops. When a non-wetting substrate is present, the impermeable wall will force the fraction of the mass that would have crossed the dashed line to move upwards, leading to the jumping motion.

The substrate is necessary to break the symmetry in the oscillation of the merged drop. However, the symmetry breaking itself is insufficient to produce jumping. For instance, the merged drop will spread on a hydrophilic substrate instead of jumping away. For jumping to take place, the adhesion between the merged drop and the substrate should be sufficiently small. Since jumping motion has mainly been reported on surfaces with a contact angle close to 180°, we make the simplifying assumption that the substrate is smooth with a contact angle of exactly 180°. Such an assumption not only removes the singularities at the moving contact line, but also eliminates the complexity associated with the surface roughness often used to generate superhydrophobicity (Quéré 2005).

Given the importance of the oscillatory motion of the merged drop (figure 2), it is instructive to review the classical results of the small-amplitude oscillation of a viscous liquid drop in a quiescent medium (Rayleigh 1879; Reid 1960; Chandrasekhar 1961). For an inviscid drop with an equilibrium radius of $r = 2^{1/3} r_0$, the fundamental frequency for a harmonic oscillation in the form of the second-degree Legendre polynomial is given by

$$f = \frac{1}{2\pi}\sqrt{\frac{8\sigma}{\rho_L r^3}} = \frac{1}{\pi \tau_{ci}}, \tag{2.1}$$

where τ_{ci} is the capillary–inertial time defined as

$$\tau_{ci} = \sqrt{\frac{\rho_L r_0^3}{\sigma}}. \tag{2.2}$$

This Rayleigh frequency corresponds to a period of $T = \pi \tau_{ci}$. In the presence of a small viscosity, the oscillation frequency is essentially unchanged and the oscillation is viscously damped with a time constant for exponential decay of

$$\tau_{\nu_L} = \frac{r^2}{5\nu_L} = 0.317 \frac{\tau_{ci}}{Oh}, \tag{2.3}$$

where $\nu_L = \mu_L/\rho_L$ is the kinematic viscosity. Note that the Ohnesorge number is based on the initial radius with $Oh = \mu_L/\sqrt{\rho_L \sigma r_0}$. For a highly viscous drop with $Oh > 0.860$, corresponding to $2\pi f r^2/\nu_L = 3.69$, the damped oscillation ceases and the perturbed drop assumes an aperiodic (over-damped) decay towards the equilibrium shape.

2.2. *Numerical methods*

Building upon our earlier work (Yue, Zhou & Feng 2006*a*; Yue *et al.* 2006*b*; Zhou *et al.* 2010), we have implemented a three-dimensional (3D) numerical simulation using the phase-field method to capture the evolution of air–liquid interfaces with rapidly changing topology. In the simulation, a phase-field variable ϕ is introduced to describe the thin but diffuse interface between the two components. Across the diffuse

	σ (mN m^{-1})	μ_L (mPa s)	μ_G (mPa s)	μ_L/μ_G	ρ_L (kg m^{-3})	ρ_{G0} (kg m^{-3})	ρ_L/ρ_{G0}	ρ_G (kg m^{-3})	ρ_L/ρ_G
20 °C	72.7	1.071	0.0182	58.8	998	(1.190)	(839)	19.96	50
100 °C	58.9	0.282	0.0219	12.9	958	(0.934)	(1026)	19.16	50

TABLE 1. The fluid properties assume literature values at either 20 °C or 100 °C, except for the air density. Owing to limited capability in resolving large density ratios, an artificial air density (ρ_G) is adopted instead of the physical air density (ρ_{G0}, parenthesized values in the table), so as to maintain a numerically meaningful density ratio of $\rho_L/\rho_G = 50$. Unless otherwise noted, the 100 °C case is assumed.

interface, ϕ changes continuously from $+1$ for the bulk liquid to -1 for the bulk air. The interfacial flow is governed by the Navier–Stokes equations and the Cahn–Hilliard equation (Yue *et al.* 2004)

$$\nabla \cdot \boldsymbol{v} = 0, \tag{2.4}$$

$$\rho\left(\frac{\partial \boldsymbol{v}}{\partial t} + \boldsymbol{v}\cdot\nabla\boldsymbol{v}\right) = -\nabla P + \mu\nabla^2\boldsymbol{v} + G\nabla\phi, \tag{2.5}$$

$$\frac{\partial \phi}{\partial t} + \boldsymbol{v}\cdot\nabla\phi = \gamma\nabla^2 G, \tag{2.6}$$

where $\boldsymbol{v}$ is the velocity vector, t is the time, P is the pressure, γ is the mobility parameter and G is the Cahn–Hilliard chemical potential (Cahn & Hilliard 1958) given by

$$G = \lambda\left[-\nabla^2\phi + \frac{(\phi^2-1)\phi}{\epsilon^2}\right]. \tag{2.7}$$

In the chemical potential, ϵ is the capillary width characterizing the thickness of the interface, and λ is the interfacial energy density related to the interfacial tension σ by

$$\sigma = \frac{2\sqrt{2}}{3}\frac{\lambda}{\epsilon}. \tag{2.8}$$

Note that the fluid properties in the diffuse interface are averaged according to the local phase-field parameter, e.g. $\rho = (1/2)(1+\phi)\rho_L + (1/2)(1-\phi)\rho_G$, where ρ_L and ρ_G are, respectively, the density of the bulk liquid and gas, and $\mu = (1/2)(1+\phi)\mu_L + (1/2)(1-\phi)\mu_G$, where μ_L and μ_G are, respectively, the viscosity of the bulk liquid and gas.

All physical quantities are non-dimensionalized by the initial drop radius (r_0), the liquid density (ρ_L) and the surface tension (σ), leading to three dimensionless parameters, the Ohnesorge number ($\mu_L/\sqrt{\rho_L\sigma r_0}$), the density ratio ($\rho_L/\rho_G$) and the viscosity ratio (μ_L/μ_G). The dimensionless variables are represented with an asterisk, e.g. $\boldsymbol{v}^* = \boldsymbol{v}/u_{ci}$ and $t^* = t/\tau_{ci}$. The physical properties for water and air are assumed to be the literature values at either 20 °C or 100 °C (table 1), in an effort to simulate fluid properties during superhydrophobic condensation or Leidenfrost experiments. The only exception is the numerical air density, which assumes a value much higher than the physical density such that $\rho_L/\rho_G = 50$; see discussions below about the numerical convergence with respect to ρ_L/ρ_G. Unless otherwise noted, the properties at 100 °C are adopted.

We have simulated the coalescence of two identical, initially static drops on a flat surface with a contact angle of 180° (figure 1). The two drops are initially situated to be tangential to each other and tangential to the supporting surface. Thus, the diffuse interfaces of the two drops initially overlap, and this may have precipitated the onset of coalescence (Yue *et al.* 2006*a*). The computational domain is a rectangular box with a dimensionless volume of $6 \times 6 \times 5$, and the xy plane is reduced to 3×3 by symmetry. A no-slip boundary condition is imposed at the bottom wall, while stress-free conditions are set on all other walls except for the two walls of symmetry. The mobility parameter is set as $\gamma^* = 10^{-5}$, a suitable value for a capillary width of $\epsilon^* = 0.05$ (Ghigliotti, Zhou & Feng 2013). The governing equations are solved by a finite-element code, AMPHI, which uses adaptive meshing to resolve the interfacial region. The mesh size at the interface is set as $h_i^* = 0.05$, and those in the bulk water and air are, respectively, 0.28 and 0.97. A non-dimensional time step of $\delta t^* = 10^{-3}$ ensures adequate temporal resolution.

Numerical convergence is mainly tested on the maximum velocity of the merged drop. For the symmetric coalescence of two identical drops, we define the instantaneous velocity of the merged drop ($\bar{v}$) by mass-averaging the z component velocity over the entire drop,

$$\bar{v} = \frac{\displaystyle\int_{\Omega} \tfrac{1}{2}(1+\phi)\rho_L v_z \,\mathrm{d}\Omega}{\displaystyle\int_{\Omega} \tfrac{1}{2}(1+\phi)\rho_L \,\mathrm{d}\Omega}, \tag{2.9}$$

where Ω represents the entire computational domain, and z is the vertical direction perpendicular to the substrate. Below we shall refer to $\bar{v}$ as simply the drop velocity. The maximum value ($\bar{v}_m$) is then extracted from the evolution of the drop velocity, $\bar{v}(t)$.

Two limitations of our numerical methods deserve discussion. (i) Our phase-field model cannot accurately handle density ratios much above $\rho_L/\rho_G = 100$. However, we have confirmed that the air density no longer matters to the results for a density ratio above 50, the default value in our simulations. For example, with $\epsilon^* = 0.05$ and $Oh = 0.003\,75$ (corresponding to $r_0 = 100$ μm for water drops at 100 °C), $\rho_L/\rho_G = 10$, 30, 50, 100 yield $\bar{v}_m^* = 0.2478$, 0.2624, 0.2691, 0.2695. The monotonic convergence is consistent with the diminishing dynamic role of the surrounding air with decreasing density. (ii) As with any diffuse-interface simulation, we must use an interfacial thickness that is small enough so that the sharp interface limit is achieved (Zhou *et al.* 2010). By shrinking the interfacial thickness and the grid size at the interface simultaneously, we have confirmed reasonable convergence to this limit for $\epsilon^* = 0.05$. For example, with $\rho_L/\rho_G = 50$ and $Oh = 0.003\,75$, $\epsilon^* = h_i^* = 0.1$, 0.075, 0.05 yield $\bar{v}_m^* = 0.2878$, 0.2616, 0.2691. Based on these results and other tests at $Oh = 0.0375$, 0.375 (corresponding to $r_0 = 1$ μm, 10 nm), the numerical error for the maximum velocity is estimated to be within 10 %.

3. Numerical results

Using the 3D numerical model, we analyse the jumping process from different perspectives and investigate the capillary–inertial velocity scaling including the viscous cutoff.

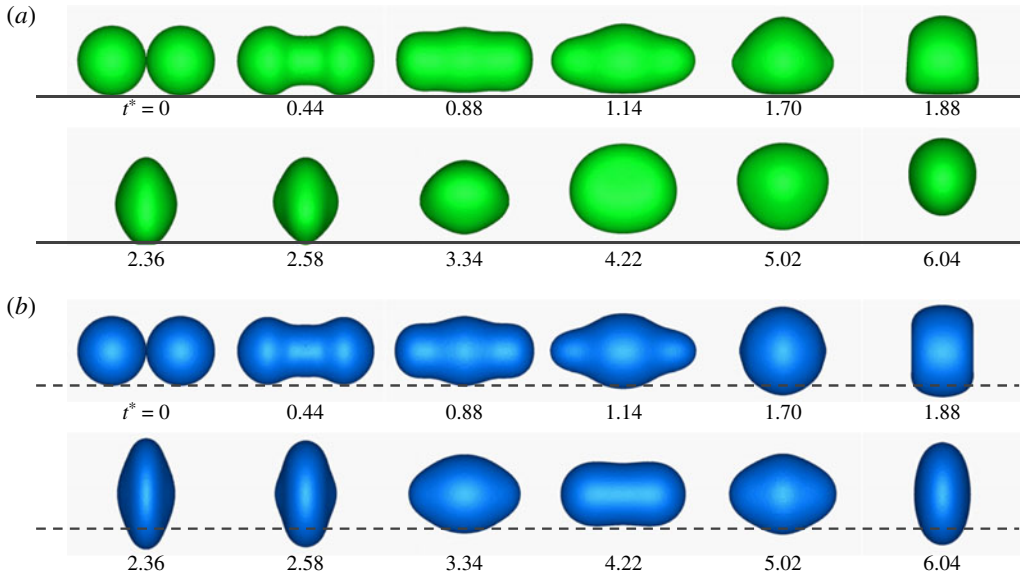

FIGURE 3. (Colour online) The 3D coalescence process of two static drops with $Oh = 0.003\,75$, $\mu_L/\mu_G = 12.9$ and $\rho_L/\rho_G = 50$. (*a*) Side *xz* view for coalescence-induced jumping on a flat substrate with a contact angle of 180°, with the substrate represented by the solid line. (*b*) Side *xz* view (or top *xy* view) of the corresponding coalescence process in the air, where the centre of mass is relocated to the centre of the computational domain. The dashed line is a visual guide for an imaginary substrate in the side view. Throughout the paper, the drop shapes resulting from coalescence on the substrate are shaded mid-grey (green online), and those in the air are dark grey (blue online). See also supplementary movies 1 and 2 available at http://dx.doi.org/10.1017/jfm.2014.320.

3.1. *Capillary–inertial jumping process*

In figure 3(*a*), the coalescence-induced jumping process is simulated with $Oh = 0.003\,75$, $\mu_L/\mu_G = 12.9$ and $\rho_L/\rho_G = 50$. These governing parameters correspond to material properties at 100 °C and an initial radius of $r_0 = 100$ μm. Note again that the numerical density ratio is smaller than the actual value of 1026 (table 1), but the difference is inconsequential based on the convergence test with respect to ρ_L/ρ_G. With such a low Ohnesorge number, the capillary–inertial process dominates and viscosity only plays a secondary role. At $t^* = 0$, the coalescence is initiated by the overlapping of diffuse interfaces. A liquid bridge forms upon coalescence and the expanding bridge reaches the substrate around 0.88, at which point the merged drop starts to experience an upward net movement. The substrate counteracts the impingement of the liquid bridge, forcing a portion of the downward-moving mass towards the sides, leading to a maximum deformation in the *x* direction at 1.14. The upward force from the substrate peaks at 1.88, beyond which the apparent contact area between the merged drop and the substrate gradually reduces towards zero at 2.58, the point of departure. The launched drop continues to oscillate while maintaining the upward motion.

In addition to the side (*xz*) view in figure 3(*a*), the capillary–inertial jumping process is also illustrated by the end (*yz*) view in figure 4(*a*) and top (*xy*) view in figure 4(*b*). Note the 3D nature of the oscillation process. For instance, the total mass is conserved

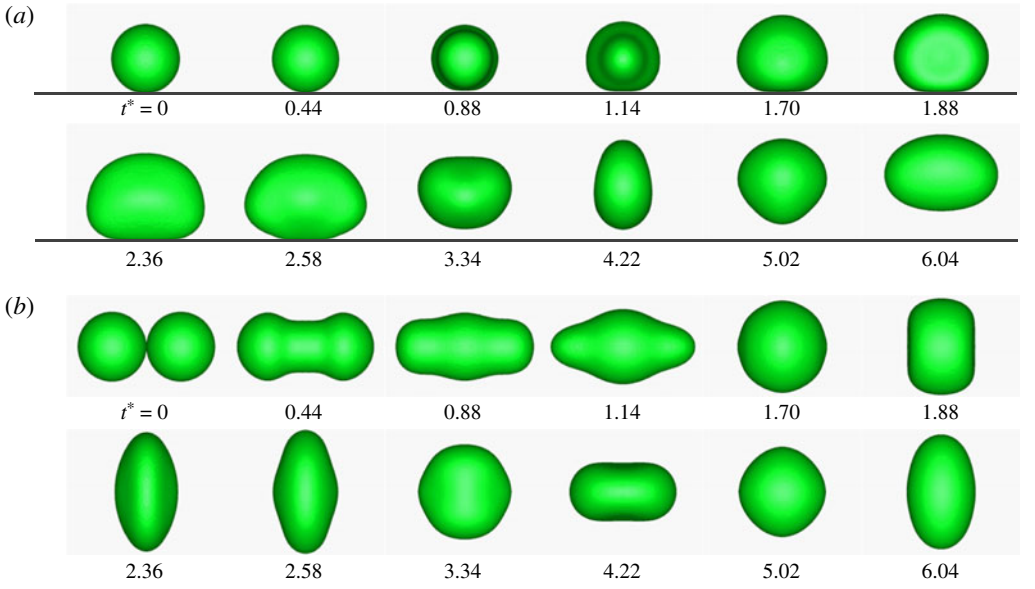

FIGURE 4. (Colour online) The jumping process in figure 3(*a*) viewed from other perspectives: (*a*) end *yz* view; (*b*) top *xy* view. The substrate visible from the end view is represented by a solid line. See also supplementary movies 3 and 4.

with a smaller footprint in one view compensated by a larger footprint from another perspective (figures 3*a* versus 4*a*).

3.1.1. *Pseudo-equilibrium configuration*

The top view with the substrate (figure 4*b*) is very similar to the drop coalescence case without the substrate (figure 3*b*). Note that the in-the-air case in figure 3(*b*) is symmetric so the top *xy* view is identical to the side *xz* view. In both figures 3(*b*) and 4(*b*), the merged drop is most rounded at approximately $t^* = 1.70$, 3.34 and 5.02, and most elongated at approximately $t^* = 2.36$, 4.22 and 6.04. The similarity indicates that the presence of the substrate only marginally alters the drop coalescence process viewed in the *xy* plane, despite significant alterations in the *xz* plane. In both figures 3(*b*) and 4(*b*), the top view of the jumping process is roughly periodic with a period close to π, which, according to (2.1), is the period for the harmonic oscillation of an unbounded spherical drop of the same volume as the merged drop.

The similarity in top view between the on-the-substrate (figure 3*b*) and in-the-air (figure 4*b*) cases is shown more quantitatively in figure 5. With a coordinate system attached to the centre of the merged mass while preserving the axial directions defined in figure 1, three quantities are extracted as the axial lengths of the merged drop: the width and height of the liquid bridge (w_y and w_z), and the length of the merged drop (w_x). Note that w_x is not necessarily the maximum extension of the merged drop in the x direction. For the drop coalescence in the air (figure 5*b*), w_x eventually assumes the same value as w_y (which equals w_z by symmetry) when the oscillation is dissipated by viscosity and the merged drop reaches a spherical shape at equilibrium with $w_x^* = w_y^* = w_z^* = 2r^* \approx 2.52$. We shall use pseudo-equilibrium to identify the shapes with $w_x^* = w_y^*$ but not yet at the final equilibrium. Similar observations can be made for drop coalescence on the substrate (figure 5*a*) with the coordinate system attached to

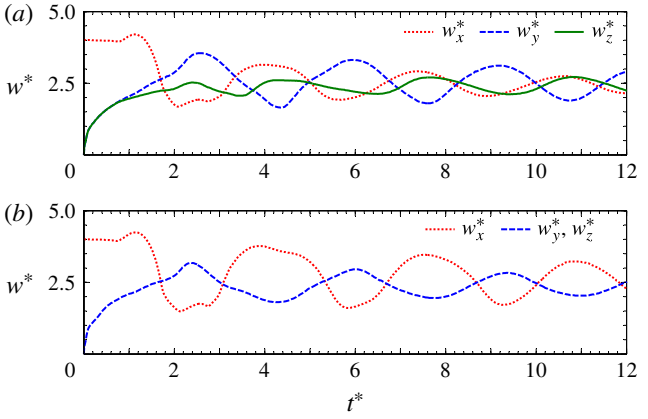

FIGURE 5. (Colour online) Evolution of the axial lengths of the merged drop, where the coordinate system is attached to the centre of mass: (*a*) on the substrate, corresponding to figures 3(*a*) and 4; and (*b*) in the air, corresponding to figure 3(*b*). Compared to the axisymmetric case in panel (*b*) with $w_y^* = w_z^*$, the presence of the substrate in panel (*a*) breaks the symmetry and also alters the x axial length (w_x^*). The shape oscillation of the merged drop is approximately periodic, with a period around π. The point of equal axial lengths in the top xy view ($w_x^* = w_y^*$) is used to identify the pseudo-equilibrium configuration.

the merged drop. The substrate breaks the symmetry so w_y^* is no longer identical to w_z^*. However, the xy view on the substrate strongly resembles that in the air judging from both the qualitative shapes (figures 3*b* and 4*b*) and the quantitative measurements of the axial lengths (figure 5*a*,*b*). This resemblance justifies our extension of the pseudo-equilibrium criterion ($w_x^* = w_y^*$) from the in-the-air case to the on-the-substrate case. Examples of pseudo-equilibrium shapes for the on-the-substrate case can be found in figures 3(*a*) and 4 at $t^* = 1.70$, 3.34 and 5.02, when the axial lengths along the moving x and y axes are equal according to figure 5(*a*).

As shown below by the energetics of the jumping process, the as-defined pseudo-equilibrium configurations approximately coincide with the local minima of the overall surface energy. The equilibrium counterpart is a spherical shape with a global minimum in surface energy. Since the condition of equal axial lengths ($w_x^* = w_y^*$) is much easier to identify numerically, we will adhere to this definition to find the pseudo-equilibrium configuration, which will prove useful below for extracting a meaningful jumping velocity.

3.1.2. *Kinematics of jumping*

To further illustrate the jumping process shown in figure 3(*a*), we plot the temporal evolution of the drop velocity defined in (2.9) in figure 6. Based on these figures, the jumping process upon coalescence can be roughly divided into four stages: (I) expansion of the liquid bridge between the coalescing drops, till approximately $t^* = 0.88$; (II) acceleration of the merged drop on the substrate, eventually reaching a maximum velocity at 2.36; (III) detachment of the merged drop from the substrate, till a complete departure at 2.58; and (IV) deceleration of the departed drop in air, where the oscillating drop relaxes towards the ultimate equilibrium shape of a sphere. Note that the slightly downward drop velocity prior to $t^* = 0.88$ is an artifact resulting

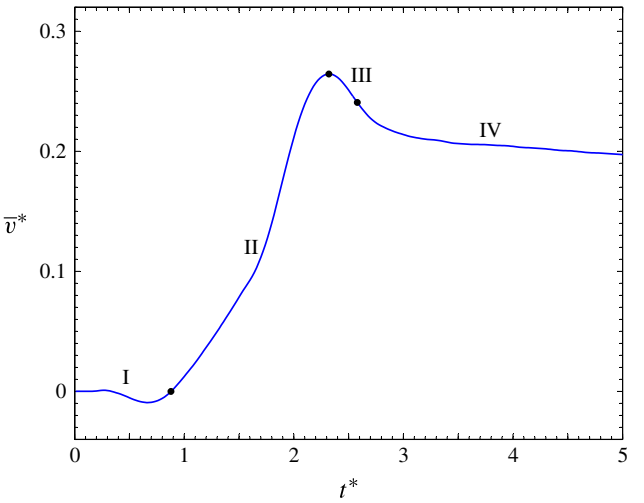

FIGURE 6. (Colour online) Evolution of the instantaneous drop velocity during the jumping process of figure 3(*a*). The $\bar{v}^*(t^*)$ curve can be divided into four regimes: I, expansion of the liquid bridge in the air; II, acceleration of the merged drop on the substrate; III, departure of the merged drop from the substrate; and IV, deceleration of the departed drop in the air.

from the initial ϕ field, which is not at equilibrium with the solid substrate (Yue, Zhou & Feng 2007). Figure 6 can be used to calculate the counter-force from the substrate as $\mathrm{d}(m\bar{v})/\mathrm{d}t$. For example, the maximum vertical force of approximately $\pi\sigma r_0$ is reached at $t = 1.88\tau_{ci}$.

The velocity field for the jumping process leading to drop detachment from the substrate is shown in figure 7. When the drops coalesce at stage I, the liquid mass is driven by capillary pressure towards the centre, leading to the expansion of the liquid bridge connecting the two initial drops. Note that the liquid bridge expands at approximately the capillary–inertial velocity (e.g. at $t^* = 0.66$) until it touches the substrate at 0.88. At stage II when the merged drop interacts with the substrate, a portion of the downward-moving liquid mass is forced to first move transversely. The x direction deformation reaches a maximum at 1.14, beyond which the oblate deformation retracts towards the pseudo-equilibrium configuration (around 1.70 in figure 3). The retracting mass is now forced to move upwards by the impermeable substrate. In this sense, the substrate enabled by capillarity effectively turns the initially downward-moving liquid mass to move upwards. At the beginning of stage III, the mass-averaged drop velocity reaches a maximum at 2.36, at which point the corresponding coalescence without the substrate would have reached the maximum extension in the prolate configuration (figure 3*b*). Beyond this point, the drop velocity actually decreases till the merged drop departs the substrate at 2.58. The decrease in drop velocity results from the low pressure underneath the drop as it is pulled away from the substrate. At stage IV, the departed drop experiences more deceleration as the cusp near the point of departure evolves towards a shape with lower curvature. After the pseudo-equilibrium point at $t^* = 3.34$ (figure 4*b*), the slight deceleration is mainly due to the drag by the external air.

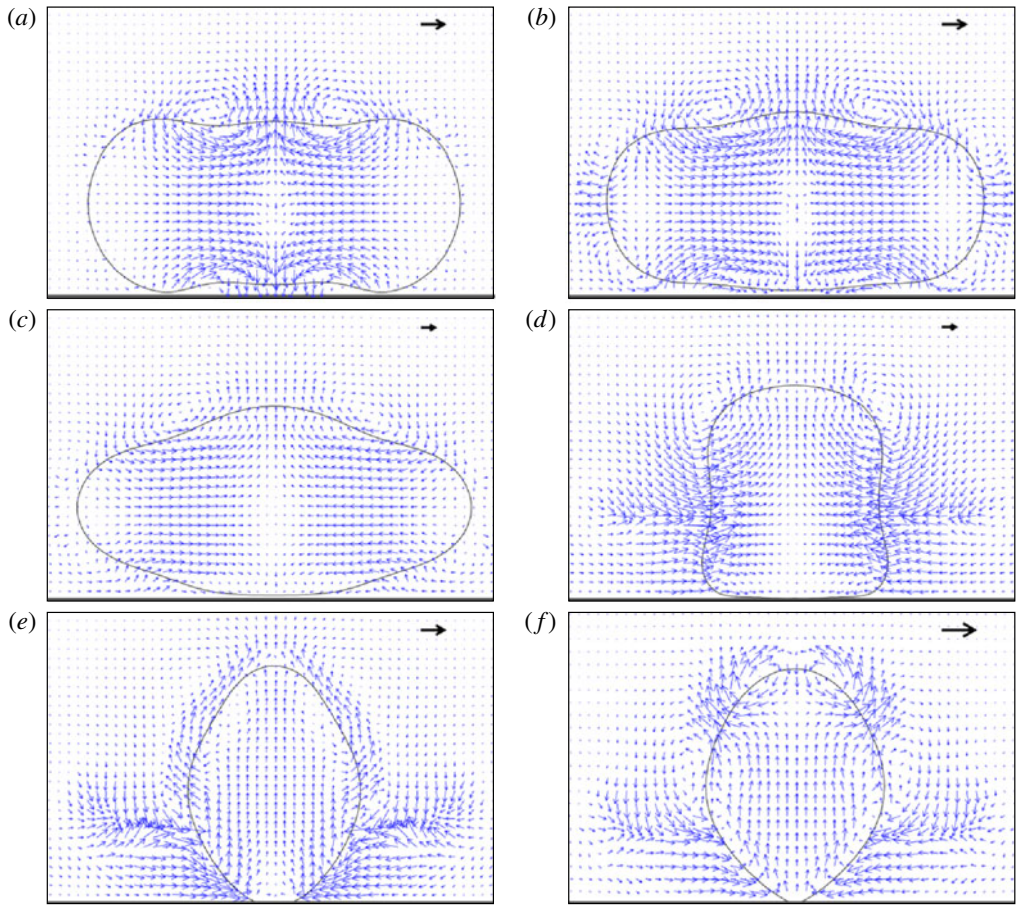

FIGURE 7. (Colour online) Instantaneous velocity fields on the symmetry plane ($y = 0$) for the jumping process in figure 3(*a*). The unit vector on the top right of each plot indicates the capillary–inertial velocity (u_{ci}). (*a*,*b*) Expansion in the air: (*a*) at $t^* = 0.66$, the boundary of the expanding bridge has a non-dimensional velocity close to unity; (*b*) at 0.88, the liquid bridge hits the substrate. (*c*,*d*) Acceleration on the substrate: (*c*) at $t^* = 1.14$, the maximal deformation in terms of extension in the x direction is reached; (*d*) at 1.88, the vertical force on the merged drop is maximum. (*e*,*f*) Departure from the substrate: from (*e*) $t^* = 2.36$ to (*f*) 2.58, the top portion of the merged drop retracts from the maximum deformation while the bottom portion lifts away from the substrate.

3.1.3. *Energetics of jumping*

Since the kinetic energy for the self-propelled jumping is converted from the surface energy released upon coalescence, additional insights can be gained by directly tracking the energy conversion process. In figure 8, the surface and kinetic energies of the merged drop are calculated by integration over the entire computational domain,

$$E_s = \int_\Omega \left[\frac{1}{2}\lambda|\nabla\phi|^2 + \frac{\lambda}{4\epsilon^2}(\phi^2 - 1)^2\right] \mathrm{d}\Omega, \tag{3.1}$$

$$E_k = \int_\Omega \frac{1+\phi}{4}\rho_L \boldsymbol{v}\cdot\boldsymbol{v}\,\mathrm{d}\Omega. \tag{3.2}$$

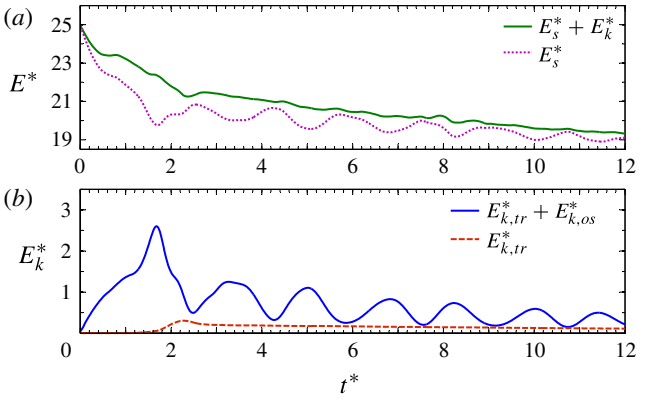

FIGURE 8. (Colour online) Surface and kinetic energy (E_s and E_k) of the merged drop during the jumping process of figure 3(*a*). The energies are non-dimensionalized by σr_0^2. (*a*) The combination of surface and kinetic energy decays over time because of viscous dissipation. The damped oscillation of energy has an approximate period of $\pi/2$. (*b*) The kinetic energy of the merged drop can be decomposed into translational and oscillatory components, $E_k = E_{k,tr} + E_{k,os}$. The oscillatory component does not contribute to any net motion and will be dissipated eventually.

Akin to the König theorem for the kinetic energy of many bodies, the kinetic energy of an isolated drop can be further decomposed by noting that $\int_\Omega \boldsymbol{v}\cdot\boldsymbol{v}\,\mathrm{d}\Omega = \int_\Omega \bar{\boldsymbol{v}}\cdot\bar{\boldsymbol{v}}\,\mathrm{d}\Omega + \int_\Omega \hat{\boldsymbol{v}}\cdot\hat{\boldsymbol{v}}\,\mathrm{d}\Omega$, where $\bar{\boldsymbol{v}}$ is the average velocity of the drop and $\hat{\boldsymbol{v}} = \boldsymbol{v} - \bar{\boldsymbol{v}}$ is the velocity with respect to the centre of mass. Given the mass-averaged drop velocity in (2.9), the translational kinetic energy for symmetric coalescence reduces to

$$E_{k,tr} = \int_\Omega \frac{1+\phi}{4}\rho_L \bar{v}^2\,\mathrm{d}\Omega. \tag{3.3}$$

In the absence of any rotational motion, the rest of the kinetic energy is attributed to the oscillatory motion, $E_{k,os} = E_k - E_{k,tr}$. As far as the self-propelled jumping is concerned, the translational kinetic energy associated with $\bar{v}$ is the only useful part, which arises from the substrate breaking the top-down symmetry of the coalescence-induced motion. For drop coalescence in the air, the ensuing motion is completely oscillatory.

Prior to coalescence, the overall surface energy (E_s) has an initial value of $8\pi\sigma r_0^2 = 25.1\sigma r_0^2$. After coalescence, the surface energy should eventually reduce to a lower value of $4\pi\sigma 2^{2/3} r_0^2 = 19.9\sigma r_0^2$ after many cycles of oscillations. As the merged drop asymptotes towards the equilibrium shape, the period of oscillation for the merged drop is expected to approach π in accordance with (2.1). Indeed, the surface energy in figure 8(*a*) exhibits damped oscillation at a period close to $\pi/2$. The local surface energy minima in figure 8 approximately coincide with the pseudo-equilibrium configurations in figure 5, where the merged drop is most rounded.

The combination of surface and kinetic energy ($E_s + E_k$) reduces over time because of viscous dissipation, mainly in the liquid phase (figure 8*a*). The dissipation is stronger during the initial merging process when compared to the oscillation process after the departure. The stronger viscous dissipation prior to departure is due to the highly localized velocity gradients resulting from the drop coalescence and its

interaction with the substrate (figure 7). After departure, the milder energy dissipation is due to viscous damping of the oscillation over the entire drop, with a viscous decay time eventually approaching $\tau_{v_L}/2$ according to (2.3). Aside from the viscous dissipation, the overall surface energy exchanges with the total kinetic energy during the capillary–inertial oscillation, evident by their antiphase variations over time. Since the translational kinetic energy ($E_{k,tr}$) is only a small fraction of the total kinetic energy and is more or less constant after departure (figure 8*b*), the energy exchange is mostly between the surface energy and the oscillatory kinetic energy ($E_{k,os}$). The oscillatory component of the kinetic energy is mainly dissipated by the internal liquid viscosity, while the translational component is mainly dissipated by the external air viscosity.

3.2. *Scaling of jumping velocities*

Next, we numerically assess the effects of viscosity by varying the Ohnesorge number defined in (1.2) and test the capillary–inertial scaling in (1.1) for the jumping velocity. As justified below, the jumping velocity ($\bar{v}_j^*$) is extracted from the computed $\bar{v}^*(t^*)$ curve at the first pseudo-equilibrium configuration after the drop departure.

3.2.1. *Viscous effects*

As the Ohnesorge number increases towards unity, viscous effects will eventually dominate over the evolution from the two-lobed initial condition towards the spherical shape at the eventual equilibrium. In figure 9(*a*) with $Oh = 0.375$, which corresponds to an initial radius of $r_0 = 10$ nm at 100 °C, the viscous effects slow down the dynamics and suppress the self-propelled jumping. The viscosity-dominated process in figure 9(*a*) is in sharp contrast to the inertia-dominated one in figure 3(*a*) with a much smaller $Oh = 0.003\,75$. Most notably, the sluggishly evolving liquid bridge no longer impinges upon the substrate, and the merged drop gradually approaches spherical equilibrium without jumping away from the substrate. The viscous slowdown is consistent with (2.3): at $Oh = 0.375$, the viscous decay time constant (τ_{v_L}) is approximately equal to the time scale (τ_{ci}) governing the capillary–inertial jumping process. The strong viscous damping is also evident from the corresponding case of drop coalescence in the air (figure 9*b*), where the merged drop stays nearly spherical beyond $t^* = 4.18$, a point of pseudo-equilibrium.

The effects of viscosity are further illustrated by the evolution of the instantaneous drop velocity, which strongly depends on the Ohnesorge number (figure 10). The Ohnesorge number is varied from $Oh = 0.001\,19$ to 0.685 with other parameters fixed at $\mu_L/\mu_G = 12.9$ and $\rho_L/\rho_G = 50$, corresponding to a variation of the initial drop radius from $r_0 = 1$ mm to 3 nm at 100 °C. With $Oh \lesssim 0.01$ ($r_0 \gtrsim 10$ μm), the $\bar{v}^*(t^*)$ curves in figure 10(*a*) are qualitatively very similar. Each curve can be divided into the four regimes illustrated in figure 6: expansion in the air, acceleration on the substrate, deceleration on and departure from the substrate, and deceleration in the air. With $0.01 \lesssim Oh \lesssim 0.3$ (10 μm $\gtrsim r_0 \gtrsim$ 10 nm), the deceleration rates during stages III and IV increase with increasing Ohnesorge number (i.e. increasing viscous effects at decreasing radius), and the curves gradually take on a different character (figure 10*b*). With $Oh \gtrsim 0.3$ ($r_0 \lesssim 10$ nm), the merged drop no longer jumps away from the substrate and the released surface energy is completely dissipated by viscosity over a short time.

The Ohnesorge number defined by (1.2) is appropriate to quantify the relative importance of viscosity to determine if the merged drop will jump away from the

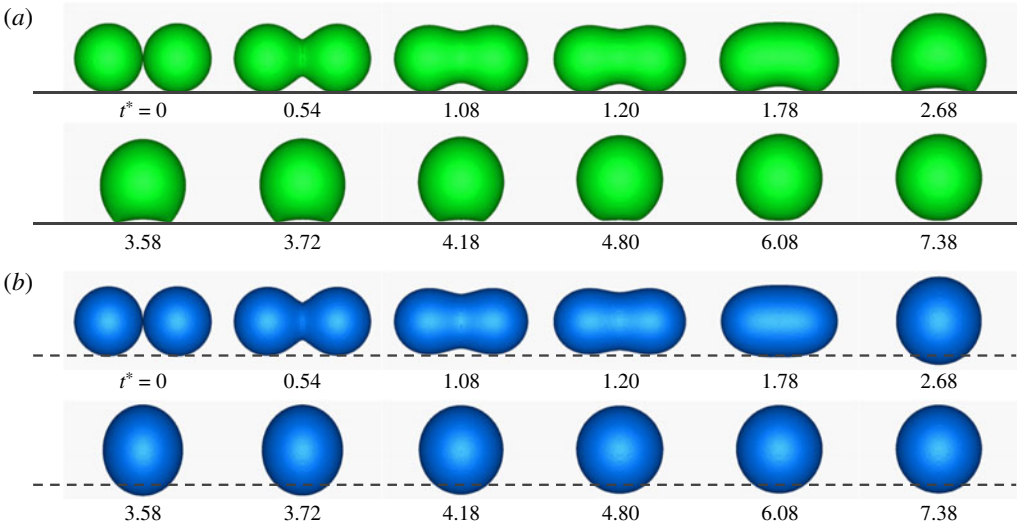

FIGURE 9. (Colour online) Side xz view of the coalescence process under conditions identical to those of figure 3 except for a larger $Oh = 0.375$: (a) on the substrate; and (b) in the air. The self-propelled jumping from the substrate is prohibited by strong viscous effects. Aided by the top xy view of the coalescence on the substrate (not shown), which is almost indistinguishable from the in-the-air case shown in panel (b), the time stamps are chosen to mirror those in figure 3 as much as possible while accounting for the viscous slowdown. See also supplementary movies 5 and 6.

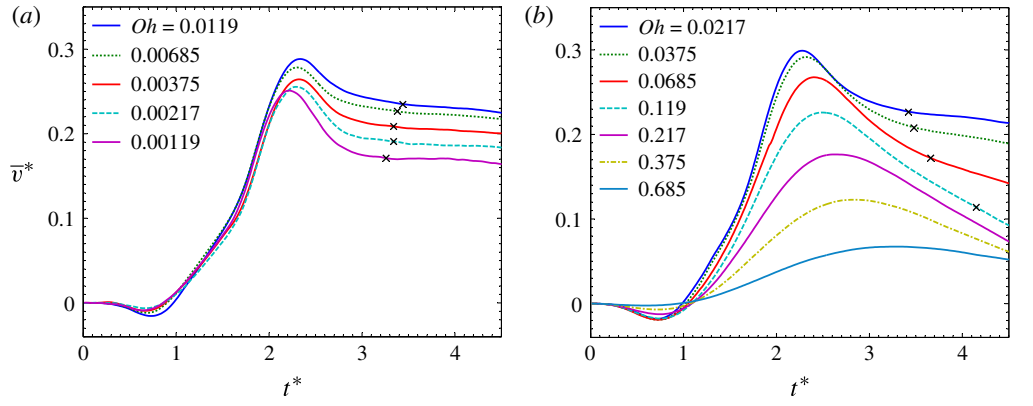

FIGURE 10. (Colour online) The evolution of the drop velocity as a function of Ohnesorge number with $\mu_L/\mu_G = 12.9$ and $\rho_L/\rho_G = 50$. (a) With $Oh \lesssim 0.01$, the $\bar{v}^*(t^*)$ curves are qualitatively similar. From top to bottom, the curves correspond respectively to $r_0 =$ 10 μm, 30 μm, 0.1 mm, 0.3 mm and 1 mm at 100 °C. (b) With $Oh \gtrsim 0.01$, the $\bar{v}^*(t^*)$ curves assume a different character with stronger viscous effects at increasing Ohnesorge numbers. From top to bottom, the curves correspond respectively to $r_0 = 3$ μm, 1 μm, 0.3 μm, 0.1 μm, 30 nm, 10 nm and 3 nm at 100 °C. The crosses indicate the first pseudo-equilibrium configuration (with equal axial lengths in the xy view) after the merged drop has departed the surface. At $Oh = 0.217$, this position is at $t^* = 5.64$ with $\bar{v}^* = 0.0149$; at $Oh = 0.375$ and 0.685, the merged drop no longer jumps away.

surface. Prior to jumping, the viscous effects are mainly due to the liquid viscosity, which is much higher than the air viscosity. In the case when the merged drop departs the surface, the external air viscosity becomes important in dissipating the translational jumping motion. This distinction is particularly relevant beyond the first pseudo-equilibrium configuration after the departure, the position indicated by the crosses in figure 10.

3.2.2. *Extraction of jumping velocities*

For the capillary–inertial regime in figure 10(*a*), although the maximum velocity ($\bar{v}_m^*$) is mathematically well defined, the merged drop has not yet left the surface ($t^* = 2.36$ in figure 3*a*). At the point of departure when the bottom of the merged drop leaves the substrate, the drop has a cusp-like shape near the bottom and the internal viscous dissipation is still strong ($t^* = 2.58$). The strong deceleration of the merged drop gradually transits to a much milder deceleration, and the point of transition approximately coincides with the first pseudo-equilibrium configuration after the departure ($t^* = 3.34$). This pseudo-equilibrium configuration is the most sensible choice for extracting the jumping velocity, since the strong deformation resulting from the interaction with the substrate has largely relaxed by then. Consistent with this justification, the pseudo-equilibrium configuration roughly marks the beginning of the nearly constant deceleration in the air (figure 10*a*), making the velocity extracted at this position most meaningful for determining the travel distance of the launched drop against air friction.

The situation is more complex for the more viscous drops in figure 10(*b*), particularly for the cases with $0.1 \lesssim Oh \lesssim 0.3$ where the merged drop eventually jumps away, but stays attached to the substrate long after it has reached the maximum velocity. In these cases, the merged drop is strongly decelerated by the surrounding air from the point of departure to the first pseudo-equilibrium configuration after the departure. Despite this caveat, the jumping velocity is still extracted at this pseudo-equilibrium configuration for consistency. We shall note that the exact jumping velocity at such high Ohnesorge numbers is of little practical interest since the strong air friction quickly brings the departed drop to rest, severely limiting the launching distance.

3.2.3. *Capillary–inertial velocity scaling and viscous cutoff*

As a function of the Ohnesorge number, the maximum velocity ($\bar{v}_m^*$) of the merged drop prior to jumping is plotted in figure 11(*a*), and the jumping velocity ($\bar{v}_j^*$) according to the aforementioned definition is shown in figure 11(*b*). To facilitate comparisons with the experiments below, we have used two sets of properties in table 1 corresponding to experiments at 100 °C and 20 °C, respectively. This property variation also offers an opportunity to vary the viscosity ratio (μ_L/μ_G) in addition to the Ohnesorge number (Oh), while the remaining governing parameter of density ratio (ρ_L/ρ_G) is kept constant. The maximum velocity is not a strong function of the external air viscosity, so $\bar{v}_m^*$ mainly varies with the Ohnesorge number, which is defined using the liquid viscosity (μ_L). On the other hand, the jumping velocity is extracted when the merged drop has already jumped into the air, so $\bar{v}_j^*$ can additionally depend on the air viscosity (μ_G) and therefore the viscosity ratio.

The jumping velocity is expected to follow the capillary–inertial scaling (1.1) with $\bar{v}_j \sim \sqrt{\sigma/(\rho_L r_0)}$. Indeed, in the capillary–inertial regime ($Oh \lesssim 0.1$), the jumping velocity is approximately constant with $\bar{v}_j^* \approx 0.2$ (figure 11*b*). In the viscous regime dominated by the liquid viscosity ($Oh \gtrsim 0.1$), a viscous cutoff to the capillary–inertial scaling is observed in figure 11(*b*) with rapidly decreasing $\bar{v}_j^*$ at increasing Oh.

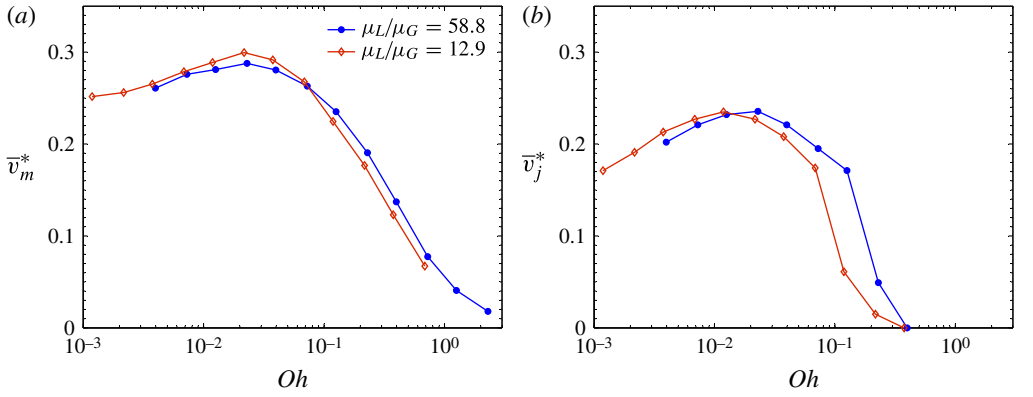

FIGURE 11. (Colour online) The velocity of the merged drop as a function of the Ohnesorge number. The viscosity ratios (μ_L/μ_G) are 12.9 and 58.8, corresponding to properties at 100 °C and 20 °C, respectively. (*a*) The maximum drop velocity ($\bar{v}_m^*$) prior to jumping; (*b*) the jumping velocity ($\bar{v}_j^*$) extracted at the first pseudo-equilibrium configuration after the drop departure.

4. Comparison with experiments

In this section, we first summarize the assumptions in our simulations and compare the numerical results with available experimental evidence, and then discuss the remaining puzzles outlined in the introduction.

4.1. *Numerical assumptions and experimental strategies*

The following assumptions have been adopted in the numerical model, roughly in order of decreasing importance. (i) The substrate has a contact angle of 180°. The drops are initially contacting the substrate but without any adhesion. (ii) The onset of coalescence is instantaneous upon contact between the diffuse interfaces. (iii) The liquid and air have constant properties, and the air density in the numerical code is set to an artificially high value owing to limitations of the phase-field code. (iv) Gravitational effects are neglected for drop radii well below the capillary length. Except for the first assumption on the boundary condition of the non-wetting surface, all other assumptions can be justified on theoretical grounds and/or with carefully designed experiments. A rigorous experimental test should also consider implied assumptions such as equal initial drop radii and negligible approaching velocity, as well as the slight ambiguity in extracting the jumping velocity; see more discussions in our companion paper (Liu *et al.* 2014*a*).

To test the key assumption on the non-wetting boundary condition, the numerical results are compared to complementary experimental data on both Leidenfrost and textured superhydrophobic surfaces. For experiments on heated Leidenfrost surfaces, water drops are floating on a vapour layer so the contact angle can be assumed to be 180° (Quéré 2013). However, the Leidenfrost drops are not directly contacting the substrate, and the thickness of the vapour layer may vary depending on the dynamic interaction between the drops and the heated substrate (Celestini, Frisch & Pomeau 2012; Liu *et al.* 2014*a*). For experiments on textured superhydrophobic surfaces, water drops are formed by cooling the surfaces below the dew point of the ambient air (Boreyko & Chen 2009; Miljkovic *et al.* 2013). The dew drops

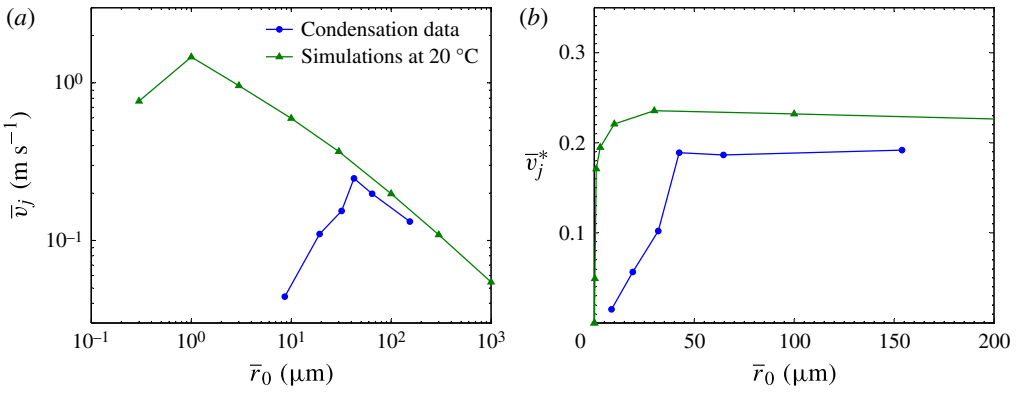

FIGURE 12. (Colour online) Comparison of numerical simulations at 20 °C with superhydrophobic jumping experiments. The experimental data are taken from Boreyko & Chen (2009), excluding asymmetric coalescence cases with larger than 33 % disparity in the radii of coalescing drops. (*a*) The $\bar{v}_j \sim r_0^{-1/2}$ power law is parallel to the diagonal line of the logarithmic graph. The viscous cutoff radius is numerically predicted to be around 0.3 μm. (*b*) The same data are replotted on a linear graph emphasizing the region around 30 μm, the experimentally identified cutoff radius on textured superhydrophobic surfaces.

exhibit a large apparent contact angle, but the contact angle is smaller than 180°, indicating a non-zero drop–surface adhesion. An additional complication arises from the roughness of a superhydrophobic substrate, which among other things gives rise to the complex interaction between the dynamic liquid drops and the air cavities within the roughened surface (Reyssat *et al.* 2010).

4.2. *Numerical results versus experimental data*

Compared to the experimental data on both Leidenfrost and superhydrophobic surfaces, our numerical model has faithfully captured the self-propelled jumping processes and confirmed the capillary–inertial scaling. The comparisons below are largely based on two sets of data. In figure 12, the experimental data are taken from Boreyko & Chen (2009), and the numerical simulations assume the fluid properties to be at 20 °C because the superhydrophobic water drops are condensed from the ambient air. In figure 13, the experimental data are taken from Liu *et al.* (2014*a*), and the numerical simulations assume the fluid properties to be at 100 °C because the Leidenfrost water drops are experiencing film boiling at atmospheric pressure.

4.2.1. *Jumping process*

The simulations capture the capillary–inertial process leading to the self-propelled motion, including the expanding bridge between the two coalescing drops, the impingement upon the substrate by the merged drop, and its eventual departure from the substrate. For experimental data that resemble the simulated process in figure 3(*a*), see for example the Leidenfrost jumping process in figure 4 of Liu *et al.* (2014*a*) and the superhydrophobic counterpart in figure 2 of Wisdom *et al.* (2013). In addition to the favourable comparison to the Leidenfrost experiments detailed in our companion paper (Liu *et al.* 2014*a*), we note that the numerically captured departure process between $t^* = 2.36$ and 2.58 in figure 3(*a*) is experimentally observed on

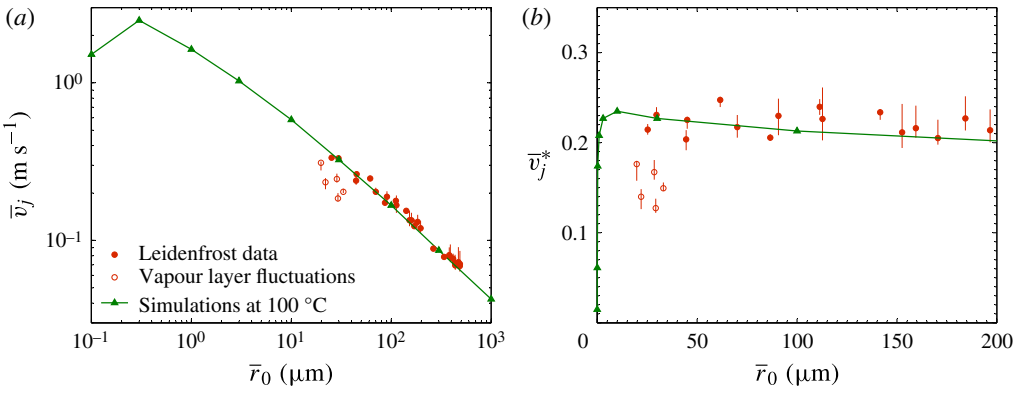

FIGURE 13. (Colour online) Comparison of numerical simulations at 100 °C with the Leidenfrost jumping experiments in Liu *et al.* (2014*a*). (*a*) The $\bar{v}_j \sim r_0^{-1/2}$ power law is parallel to the diagonal line of the logarithmic graph. The viscous cutoff radius is numerically predicted to be around 0.1 μm. (*b*) The same data are replotted on a linear graph emphasizing the region around 20 μm, the lower bound of experimentally accessible radii because of spontaneous fluctuations of the vapour layer thickness. The reduction in the jumping velocity for the data points represented by open symbols is a result of the vapour layer fluctuation, not an indication of a cutoff radius.

superhydrophobic surfaces by Wisdom *et al.* (2013) between 200 and 240 μs in their figure 2.

The simulations predict the duration from initial coalescence to the jumping departure (T_j) to be close to $2.5\tau_{ci}$ based on figures 3(*a*) and 10(*a*). For Leidenfrost surfaces, the agreement is apparent by comparing the experiments and simulations with the same time stamps (figures 4 and 6 in Liu *et al.* (2014*a*)). For superhydrophobic surfaces, the agreement is also good: for an average drop radius of $\bar{r}_0 = 235$ μm ($\tau_{ci} = 0.42$ ms), the measured duration is $T_j = 1.0 \pm 0.2$ ms from figure 4 and the associated video in Boreyko & Chen (2009); the empirical formula from our numerical results yields $T_j \approx 2.5\tau_{ci} = 1.1$ ms.

4.2.2. *Capillary–inertial scaling*

Before comparing the numerical and experimental data regarding the scaling of jumping velocities, we shall note that the power law of $\bar{v}_j \sim r_0^{-1/2}$ in (1.1) is best tested in a log–log plot. For example, an order-of-magnitude mismatch in the cutoff radius apparent in the logarithmic plot (figure 12*a*) can be obscured by the linear plot (figure 12*b*). Indeed, *ad hoc* forms of viscous dissipation can lead to a seemingly reasonable fit to experimental data in a linear plot; see for example Wang *et al.* (2011). To avoid this pitfall, we plot the data in both logarithmic and linear scales in figures 12 and 13.

In figures 12(*a*) and 13(*a*), the $\bar{v}_j \sim r_0^{-1/2}$ scaling trend is shown by the numerical jumping velocities based on figure 11(*b*). As long as the drop radius is above the viscous cutoff, the simulations yield a nearly constant non-dimensional jumping velocity ($\bar{v}_j^*$) of around 0.2 (figures 12*b* and 13*b*). Experimentally, the $\bar{v}_j \sim r_0^{-1/2}$ power law is confirmed by measurements on both superhydrophobic and Leidenfrost surfaces, and an approximately constant velocity of $\bar{v}_j^* \approx 0.2$ is indeed observed on both surfaces.

On superhydrophobic surfaces, the measured jumping velocities are somewhat lower than numerical predictions (figure 12*b*), which is expected because of the non-zero adhesion between the coalescing drops and the substrates. On Leidenfrost surfaces, the measured values nearly match the numerical predictions within experimental uncertainty (figure 13*b*). The measured jumping velocities are slightly but consistently higher, which can perhaps be explained by the enhanced vaporization of the merged drop as the heated substrate reacts to its impingement.

4.2.3. *Cutoff radius*

The simulations predict a viscous cutoff radius around 0.3 μm at 20 °C (figure 12*a*) and around 0.1 μm at 100 °C (figure 13*a*), below which the capillary–inertial scaling no longer holds. The viscous cutoff radius is two orders of magnitude lower than the experimentally identified cutoff of 30 μm on textured superhydrophobic surfaces (Boreyko & Chen 2009). To investigate this discrepancy, we have studied the self-propelled jumping on Leidenfrost surfaces, which offer a better approximation to our simplified boundary condition (Liu *et al.* 2014*a*).

The Leidenfrost data indicate no obvious cutoff in the accessible range of radii as detailed in Liu *et al.* (2014*a*). For Leidenfrost experiments, the lower limit of the initial drop radii is approximately 20 μm, around which the vapour layer thickness starts to fluctuate spontaneously (Celestini *et al.* 2012; Liu *et al.* 2014*a*). The spontaneous fluctuation stems from the small radius and thus the tiny drop weight, which will be overwhelmed by the evaporative vapour flow until the liquid drop is much farther away from the heated surface (Celestini *et al.* 2012). As long as the vapour layer thickness is not affected by this spontaneous fluctuation, the measured jumping velocity closely follows the numerical prediction with the initial radius down to 20 μm (figure 13). Although the viscous cutoff radius cannot be experimentally probed on Leidenfrost surfaces, the available experimental facts are entirely consistent with the numerical results. This agreement supports the adequacy of our numerical model, particularly the simplified boundary condition of a flat non-wetting surface, as a first approximation to the self-propelled jumping.

Considering the consistency between the Leidenfrost experiments and the numerical simulations, the large cutoff radius measured on textured superhydrophobic surfaces is most likely to be due to effects not captured by the simplified boundary condition. For example, the contact angle between the drops and the textured surfaces is well below 180°, indicating finite adhesion (Mognetti, Kusumaatmaja & Yeomans 2010; Reyssat *et al.* 2010) that has been ignored in the numerical model. The finite adhesion is particularly relevant for the condensate drops used in figure 12 (Miljkovic, Enright & Wang 2012; Rykaczewski *et al.* 2012*a*). The coalescing drops are also interacting with surface cavities that give rise to the superhydrophobicity. Such an interaction can be strongly dissipative (Gao & Feng 2009; Tsai *et al.* 2011), particularly as the drop radius approaches the dimensions of the cavities, which are typically of micrometre scale. In addition to the dependence on the Ohnesorge number, the cutoff radius is likely to be dependent on multiple factors, including the Young's contact angle and the geometry of the micro- and/or nano-texture. We stress that the cutoff radius is not necessarily dictated by the dimension of the micro-textures on the superhydrophobic surfaces. In Boreyko & Chen (2009), which uses 'structure B_{mn}' in Chen *et al.* (2007), the observed critical radius of around 30 μm is coincidentally close to the micropillar separation of 16 μm. As shown in Chen *et al.* (2007), the critical radius will change dramatically if the surface coating is altered or the nano-tier roughness is removed, even though the micro-tier roughness remains the same.

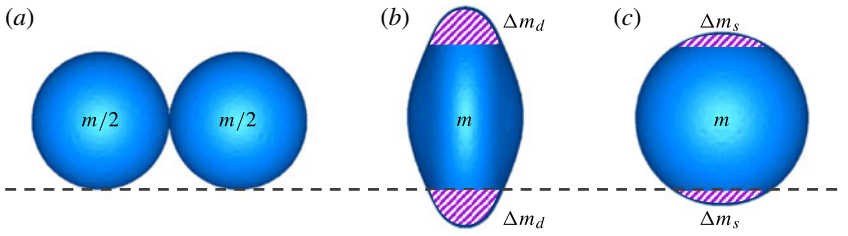

FIGURE 14. (Colour online) The symmetry-breaking action of the substrate can be estimated by the drop coalescence cases in the air. (*a*) Coalescence of two static drops of initial radius r_0, each with a mass of $m/2$. (*b*) For the maximum capillary–inertial deformation of the merged drop ($t^* = 2.36$ in figure 3*b*), the dynamic crossing mass that passes below the imaginary substrate is $\Delta m_d = 9.4\,\% m$. (*c*) For an equilibrium drop, the static crossing mass is $\Delta m_s = 3.0\,\% m$. Note that the unbalanced counter-mass associated with the broken symmetry is also labelled.

4.3. *Mechanism of low non-dimensional velocity*

Equipped with the numerical simulations, which agree well with experiments, we are now in a position to offer an explanation to the low non-dimensional jumping velocity.

4.3.1. *Symmetry-breaking mass fraction*

The self-propelled jumping results from the counter-action of the non-wetting substrate to the oscillation of the merged drop, which breaks the symmetry of the surface energy release (figure 2). This physical model is indeed supported by the experimentally validated simulations. The role of the substrate in intercepting the oscillating drop is evident by comparing the in-the-air coalescence in figure 3(*b*) and the on-the-substrate case in figure 3(*a*). As further illustrated by the flow fields in figure 7, the substrate essentially forces the downward-moving mass to eventually move upwards. The direction change is facilitated by the capillarity of the merged drop, first 'absorbing' the downward momentum through lateral deformation ($t^* = 1.14$), and then squeezing the fluid back ($t^* = 1.88$) and finally upwards ($t^* = 2.36$). Another insight from figure 7 ($t^* = 0.66$) is that the boundary of the expanding liquid bridge moves at approximately the capillary–inertial velocity (u_{ci}), which is true as long as the Ohnesorge number is much smaller than unity.

The non-dimensional jumping velocity of $\bar{v}_j^* \approx 0.2$ in the capillary–inertial regime can be rationalized by the following heuristic argument (figure 14). Based on the numerical solution of the control case without the substrate, a maximum of 9.4 % of the total mass (m) crosses the imaginary substrate represented by the dashed line when the merged drop extends to the maximum prolate configuration, i.e. $\Delta m_d \approx 10\,\% m$ in figure 14(*b*). The presence of the substrate forces a lumped mass of Δm_d that initially moves downwards at approximately u_{ci} to eventually 'bounce' upwards, in a manner analogous to the elastic rebound of entire drops on superhydrophobic surfaces (Richard & Quéré 2000). At the same time, the 'unbalanced' counter-mass of Δm_d on top of the merged drop continues to move upwards at approximately u_{ci} (from $t^* = 0.88$ onwards in figure 7). As a result of the substrate breaking the symmetry of the surface energy release, two chunks of liquid, each with a mass of Δm_d (figure 14*b*), are forced by the substrate to move upwards at the capillary–inertial velocity, while the rest of the drop still maintains the approximate top-down symmetry (figure 7). Effectively, the non-wetting substrate provides a

vertical impulse $J_z \sim 2\Delta m_d u_{ci}$. When the vertical momentum is distributed over the total drop mass, the mass-averaged jumping velocity can be approximated as

$$\bar{v}_j \sim \frac{J_z}{m} \sim \frac{2\Delta m_d}{m} u_{ci}. \tag{4.1}$$

Accordingly, the non-dimensional velocity is approximated by the dynamic symmetry-breaking mass fraction, $\bar{v}_j^* \sim 2\Delta m_d/m \approx 0.2$.

Although the dynamic crossing mass of $\Delta m_d \approx 10\,\% m$ arises from numerical simulations, we shall note that Δm_d is lower-bounded by a static crossing mass (Δm_s) from a geometric consideration (figure 14*c*). For the merged drop at final equilibrium, the static crossing mass is proportional to the volume of a spherical cap with a radius of $r = 2^{1/3} r_0$ and a height of $h_c = r - r_0$, and therefore

$$\frac{\Delta m_s}{m} = \frac{\frac{1}{3}\pi\rho_L h_c^2 (3r - h_c)}{\frac{4}{3}\pi\rho_L r^3} = \frac{(2^{1/3} - 1)^2 (2^{4/3} + 1)}{4} = 0.03. \tag{4.2}$$

In fact, this (quasi-)static crossing mass should approximate very well the sluggish movement at relatively large Ohnesorge number that is still below the critical value noted at the end of § 2.1. Indeed, the static symmetry-breaking mass fraction ($2\Delta m_s/m$) explains the displacement leading to a maximum drop velocity ($\bar{v}_m^*$) of close to 0.06 for the viscously dominated drop (e.g. $Oh = 0.685$ in figure 10*b*), even though it does not eventually jump up.

The above heuristic argument is far from rigorous, but it does offer some insights into the self-propelled jumping mechanism. We stress that the small non-dimensional jumping velocity is due to the mechanical role of the substrate in intercepting only a small fraction of the oscillating drop (figure 14). This physical insight is further supported by simulations with the substrate relocated below the coalescing drops and intercepting an even smaller fraction of mass (figure 15 inset). With increasing separation (h^*) between the substrate and the bottom of the coalescing drops, the liquid bridge impingement is delayed and the jumping velocity is reduced, until $h^* \approx 0.6$, beyond which the oscillating drop no longer makes contact with the substrate. In figure 15, the jumping velocity ($\bar{v}_j^*$) with increasing separation closely follows the dynamic symmetry-breaking mass fraction ($2\Delta m_d/m$) according to (4.1). In a sense, our heuristic model has a predictive power given the computed shape with maximum vertical deformation in the air.

4.3.2. *Discussion*

For the self-propelled jumping on non-wetting substrates, the energy conversion efficiency is low when the useful translational kinetic energy ($E_{k,tr}$) is compared to the released surface energy (ΔE_s). The low efficiency is directly related to the small non-dimensional jumping velocity, since $E_{k,tr}/\Delta E_s \approx \bar{v}_j^{*2}$ as discussed around (1.1). Most of the released surface energy is viscously dissipated, including the majority of the energy that is first stored in the oscillatory motion (figure 8). Since the translational kinetic energy is only a small fraction, it is important to decompose the kinetic energy into translational and oscillatory components. Otherwise, the energy conversion efficiency appears artificially large as reported in Nam *et al.* (2013).

The details of the flow field are ignored in our heuristic model with the lumped equation (4.1). To probe the role of the internal flow, we run simulations with the velocity field reinitialized at a particular moment. For example, at $t^* = 0.88$ when

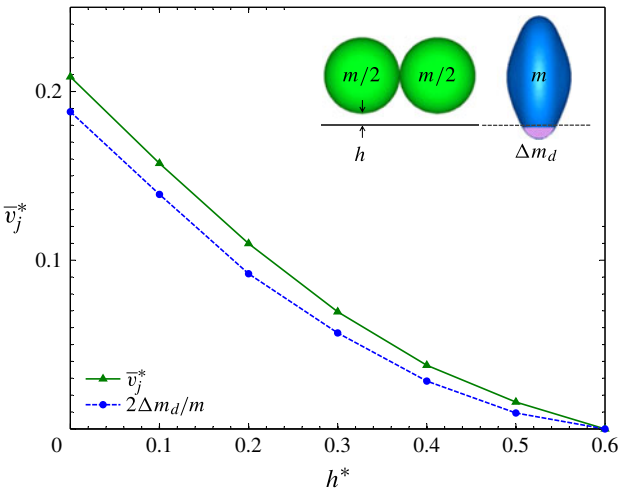

FIGURE 15. (Colour online) Non-dimensional jumping velocity ($\bar{v}_j^*$) and the dynamic symmetry-breaking mass fraction ($2\Delta m_d/m$) as a function of the separation from the substrate (h^*); the conditions are otherwise the same as those of figure 3. The inset defines the crossing mass (Δm_d), the portion of the maximum prolate deformation in the air that is intercepted by an imaginary line situated at the same position as the substrate.

the liquid bridge impingement first occurs, all the velocity field (including that on the air side) is reset to zero but the shape of the merged drop is left intact. After this reinitialization, the simulation proceeds as usual. The reinitialization at $t^* = 0.88$ delays the jumping process slightly, but the ultimate jumping velocity is nearly unchanged. Note that the velocity field is almost entirely oscillatory at $t^* = 0.88$ because of the lack of interaction with the substrate. For any other instant prior to departure, a similar reinitialization procedure is adopted, with only the oscillatory component turned off while the translational component is kept intact; the resulting jumping velocity is within 20 % of the unmodified case. These additional simulations are in line with figure 8: although the oscillatory motion dominates the kinetic energy, it is largely dissipated in the end. The detailed flow field can therefore be neglected in our derivation of (4.1), which is a lumped model for the translational jumping velocity. On the other hand, we should note that the oscillatory motion is only turned off at a selected moment (such at $t^* = 0.88$), and the oscillation is playing an obvious role in the evolution towards the drop shape at that particular moment, as well as the subsequent shape evolution after the reinitialization. Accordingly, the capillary–inertial velocity (u_{ci}) characterizing the oscillatory motion has its role in the lumped model.

Although our heuristic model borrows the concept of elastic rebound from drop impact on non-wetting surfaces (Quéré 2005), the drop impact associated with coalescence-induced jumping is markedly different. (i) Prior studies usually deal with the impact of individual drops with a uniform incoming velocity that is entirely translational, while the self-propelled jumping results from drop coalescence with highly non-uniform internal velocity that is entirely oscillatory prior to impingement. (ii) Judging from the restitution coefficient, which is the rebound velocity over the impacting velocity, the impact of individual drops on non-wetting surfaces is elastic (i.e. no appreciable loss in energy) for low-Weber-number cases (Richard & Quéré 2000) and inelastic for high-Weber-number cases (Clanet *et al.* 2004). In contrast,

the coalescence-induced jumping is always dissipative and the 'rebound' is limited to a fraction of the mass ($2\Delta m_d$), even though the capillarity-driven impingement is inherently at a low Weber number (Liu *et al.* 2014*a*, § 3.4). (iii) For the elastic rebound of individual drops upon impact, kinetic energy is first absorbed and then released through surface deformation, but the rebounded drop has the same surface energy as the incoming drop. For the coalescence-induced jumping, surface energy is released upon coalescence, so the merged drop always carries a lower surface energy compared to that of the initial drops. Part of the released energy powers the jumping motion, and the rest is (eventually) dissipated.

5. Conclusions

We have numerically simulated the 3D self-propelled jumping process upon drop coalescence on a flat non-wetting surface with a contact angle of 180°. The simulations compare favourably with experiments on both superhydrophobic and Leidenfrost surfaces. The agreement supports the physical model viewing the initial state as a two-lobed perturbation to the eventual equilibrium shape of a larger spherical drop. The jumping velocity follows the capillary–inertial scaling, as long as the drop radius is above the viscous cutoff radius. The numerically predicted cutoff radius is of the order of 0.1 μm, which is consistent with available Leidenfrost data. The consistency suggests that the much larger cutoff radius observed on textured superhydrophobic surfaces is probably a result of the complex drop–surface interaction, which is not captured by the perfectly smooth boundary condition without any drop–surface adhesion.

Based on drop coalescence processes with and without the substrate, the out-of-plane jumping results from the non-wetting substrate interfering with the oscillation of the merged drop. Excellent agreement is found for the non-dimensional jumping velocity, which is approximately 0.2. The relatively small velocity is attributed to the substrate only intercepting a small fraction of the oscillating drop. Consequently, only a tiny fraction of the released surface energy is converted into translational kinetic energy for the upward motion, the rest being stored in oscillatory modes and eventually dissipated.

Acknowledgements

F.L. and C.H.C. were supported by the National Science Foundation (CBET-08-46705 and CBET-12-36373) and the Defense Advanced Research Projects Agency (N66001-10-1-4048). G.G. and J.J.F. were supported by the Canada Research Chair program, Natural Sciences and Engineering Research Council (Discovery and Strategic grants and Accelerator Supplement), and the Canada Foundation for Innovation. The authors acknowledge Y. Zhao and B. Goldman for their work at the initial phase of the project. C.H.C. is grateful to J. Dolbow and J. Sanders for helpful discussions on numerical issues, to J. Rose for pointing out the German reference on jumping mercury drops, to T. Tan for suggesting the idea of symmetry breaking, and to D. Quéré for questioning the low but constant energy conversion efficiency. F.L. and G.G. contributed equally to this work.

Supplementary movies

Supplementary movies are available at http://dx.doi.org/10.1017/jfm.2014.320.

REFERENCES

ANDRIEU, C., BEYSENS, D. A., NIKOLAYEV, V. S. & POMEAU, Y. 2002 Coalescence of sessile drops. *J. Fluid Mech.* **453**, 427–438.

BASARAN, O. A. 1992 Nonlinear oscillations of viscous liquid drops. *J. Fluid Mech.* **241**, 169–198.

BENILOV, E. S. & VYNNYCKY, M. 2013 Contact lines with a 180° contact angle. *J. Fluid Mech.* **718**, 481–506.

BOREYKO, J. B. & CHEN, C. H. 2009 Self-propelled dropwise condensate on superhydrophobic surfaces. *Phys. Rev. Lett.* **103**, 184501.

BOREYKO, J. B. & CHEN, C. H. 2010 Self-propelled jumping drops on superhydrophobic surfaces. *Phys. Fluids* **22**, 091110.

BOREYKO, J. B. & CHEN, C. H. 2013 Vapor chambers with jumping-drop liquid return from superhydrophobic condensers. *Intl J. Heat Mass Transfer* **61**, 409–418.

BOREYKO, J. B. & COLLIER, C. P. 2013 Delayed frost growth on jumping-drop superhydrophobic surfaces. *ACS Nano* **7**, 1618–1627.

BOREYKO, J. B., ZHAO, Y. & CHEN, C. H. 2011 Planar jumping-drop thermal diodes. *Appl. Phys. Lett.* **99**, 234105.

CAHN, J. W. & HILLIARD, J. E. 1958 Free energy of a nonuniform system. I. Interfacial free energy. *J. Chem. Phys.* **28**, 258–267.

CELESTINI, F., FRISCH, T. & POMEAU, Y. 2012 Take off of small Leidenfrost droplets. *Phys. Rev. Lett.* **109**, 034501.

CHANDRASEKHAR, S. 1961 *Hydrodynamic and Hydromagnetic Stability*. Dover.

CHEN, C. H., CAI, Q., TSAI, C., CHEN, C. L., XIONG, G., YU, Y. & REN, Z. F. 2007 Dropwise condensation on superhydrophobic surfaces with two-tier roughness. *Appl. Phys. Lett.* **90**, 173108.

CHENG, J., VANDADI, A. & CHEN, C. L. 2012 Condensation heat transfer on two-tier superhydrophobic surfaces. *Appl. Phys. Lett.* **101**, 131909.

CLANET, C., BÉGUIN, C., RICHARD, D. & QUÉRÉ, D. 2004 Maximal deformation of an impacting drop. *J. Fluid Mech.* **517**, 199–208.

DIETZ, C., RYKACZEWSKI, K., FEDOROV, A. G. & JOSHI, Y. 2010 Visualization of droplet departure on a superhydrophobic surface and implications to heat transfer enhancement during dropwise condensation. *Appl. Phys. Lett.* **97**, 033104.

EGGERS, J., LISTER, J. R. & STONE, H. A. 1999 Coalescence of liquid drops. *J. Fluid Mech.* **401**, 293–310.

ENRIGHT, R., MILJKOVIC, N., AL-OBEIDI, A., THOMPSON, C. V. & WANG, E. N. 2012 Condensation on superhydrophobic surfaces: the role of local energy barriers and structure length scale. *Langmuir* **28**, 14424–14432.

FENG, J., PANG, Y., QIN, Z., MA, R. & YAO, S. 2012 Why condensate drops can spontaneously move away on some superhydrophobic surfaces but not on others. *ACS Appl. Mater. Interfaces* **4**, 6618–6625.

GAO, P. & FENG, J. J. 2009 Enhanced slip on a patterned substrate due to depinning of contact line. *Phys. Fluids* **21**, 102102.

GHIGLIOTTI, G., ZHOU, C. & FENG, J. J. 2013 Simulations of the breakup of liquid filaments on a partially wetting solid substrate. *Phys. Fluids* **25**, 072102.

HE, M., ZHOU, X., ZENG, X., CUI, D., ZHANG, Q., CHEN, J., LI, H., WANG, J., CAO, Z., SONG, Y. & JIANG, L. 2012 Hierarchically structured porous aluminum surfaces for high-efficient removal of condensed water. *Soft Matt.* **8**, 6680–6683.

HELBIG, R., NICKERL, J., NEINHUIS, C. & WERNER, C. 2011 Smart skin patterns protect springtails. *PLoS One* **6**, e25105.

HERNÁNDEZ-SÁNCHEZ, J. F., LUBBERS, L. A., EDDI, A. & SNOEIJER, J. H. 2012 Symmetric and asymmetric coalescence of drops on a substrate. *Phys. Rev. Lett.* **109**, 184502.

HUH, C. & SCRIVEN, L. E. 1971 Hydrodynamic model of steady movement of a solid/liquid/fluid contact line. *J. Colloid Interface Sci.* **35**, 85–101.

KAPUR, N. & GASKELL, P. H. 2007 Morphology and dynamics of droplet coalescence on a surface. *Phys. Rev.* E **75**, 056315.

KOLLERA, M. & GRIGULL, U. 1969 Über das Abspringen von Tropfen bei der Kondensation von Quecksilber (The bouncing off phenomenon of droplets with condensation of mercury). *Wärme- und Stoffübertragung (Heat Mass Transfer)* **2**, 31–35.

LEE, M. W., KANG, D. K., YOON, S. S. & YARIN, A. L. 2012 Coalescence of two drops on partially wettable substrates. *Langmuir* **28**, 3791–3798.

LEIDENFROST, J. G. 1756 *De Aquae Communis Nonnullis Qualitatibus Tractatus*. Johann Straube, Duisburg (translation: 1966 *Intl J. Heat Mass Transfer* **9**, 1153–1166).

LIU, F., GHIGLIOTTI, G., FENG, J. J. & CHEN, C.-H. 2014*a* Self-propelled jumping upon drop coalescence on Leidenfrost surfaces. *J. Fluid Mech.* **752**, 22–38.

LIU, T. Q., SUN, W., SUN, X. Y. & AI, H. R. 2012 Mechanism study of condensed drops jumping on super-hydrophobic surfaces. *Colloids Surf.* A **414**, 366–374.

LIU, X., CHENG, P. & QUAN, X. 2014*b* Lattice Boltzmann simulations for self-propelled jumping of droplets after coalescence on a superhydrophobic surface. *Intl J. Heat Mass Transfer* **73**, 195–200.

LV, C., HAO, P., YAO, Z., SONG, Y., ZHANG, X. & HE, F. 2013 Condensation and jumping relay of droplets on lotus leaf. *Appl. Phys. Lett.* **103**, 021601.

MENCHACA-ROCHA, A., MARTÍNEZ-DÁVALOS, A., NÚÑEZ, R., POPINET, S. & ZALESKI, S. 2001 Coalescence of liquid drops by surface tension. *Phys. Rev.* E **63**, 046309.

MERTANIEMI, H., FORCHHEIMER, R., IKKALA, O. & RAS, R. H. A. 2012 Rebounding droplet–droplet collisions on superhydrophobic surfaces: from the phenomenon to droplet logic. *Adv. Mater.* **24**, 5738–5743.

MILJKOVIC, N., ENRIGHT, R., NAM, Y., LOPEZ, K., DOU, N., SACK, J. & WANG, E. N. 2013 Jumping-droplet-enhanced condensation on scalable superhydrophobic nanostructured surfaces. *Nano Lett.* **13**, 179–187.

MILJKOVIC, N., ENRIGHT, R. & WANG, E. N. 2012 Effect of droplet morphology on growth dynamics and heat transfer during condensation on superhydrophobic nanostructured surfaces. *ACS Nano* **6**, 1776–1785.

MILJKOVIC, N. & WANG, E. N. 2013 Condensation heat transfer on superhydrophobic surfaces. *MRS Bull.* **38**, 397–406.

MOGNETTI, B. M., KUSUMAATMAJA, H. & YEOMANS, J. M. 2010 Drop dynamics on hydrophobic and superhydrophobic surfaces. *Faraday Discuss.* **146**, 153–165.

NAM, Y., KIM, H. & SHIN, S. 2013 Energy and hydrodynamic analyses of coalescence-induced jumping droplets. *Appl. Phys. Lett.* **103**, 161601.

NILSSON, M. A. & ROTHSTEIN, J. P. 2011 The effect of contact angle hysteresis on droplet coalescence and mixing. *J. Colloid Interface Sci.* **363**, 646–654.

ORME, M. 1997 Experiments on droplet collisions, bounce, coalescence and disruption. *Prog. Energy Combust. Sci.* **23**, 65–79.

PAULSEN, J. D., BURTON, J. C. & NAGEL, S. R. 2011 Viscous to inertial crossover in liquid drop coalescence. *Phys. Rev. Lett.* **106**, 114501.

PENG, B., WANG, S., LAN, Z., XU, W., WEN, R. & MA, X. 2013 Analysis of droplet jumping phenomenon with lattice Boltzmann simulation of droplet coalescence. *Appl. Phys. Lett.* **102**, 151601.

QIAN, J. & LAW, C. K. 1997 Regimes of coalescence and separation in droplet collision. *J. Fluid Mech.* **331**, 59–80.

QUÉRÉ, D. 2005 Non-sticking drops. *Rep. Prog. Phys.* **68**, 2495–2532.

QUÉRÉ, D. 2013 Leidenfrost dynamics. *Annu. Rev. Fluid Mech.* **45**, 197–215.

RAYLEIGH, LORD 1879 On the capillary phenomena of jets. *Proc. R. Soc. Lond.* **29**, 71–97.

REID, W. H. 1960 The oscillations of a viscous liquid drop. *Q. Appl. Maths* **18**, 86–89.

REYSSAT, M., RICHARD, D., CLANET, C. & QUÉRÉ, D. 2010 Dynamical superhydrophobicity. *Faraday Discuss.* **146**, 19–33.

RICHARD, D. & QUÉRÉ, D. 2000 Bouncing water drops. *Europhys. Lett.* **50**, 769–775.

RISTENPART, W. D., MCCALLA, P. M., ROY, R. V. & STONE, H. A. 2006 Coalescence of spreading droplets on a wettable substrate. *Phys. Rev. Lett.* **97**, 064501.

RYKACZEWSKI, K., OSBORN, W. A., CHINN, J., WALKER, M. L., SCOTT, J. H. J., JONES, W., HAO, C., YAO, S. & WANG, Z. 2012*a* How nanorough is rough enough to make a surface superhydrophobic during water condensation? *Soft Matt.* **8**, 8786–8794.

RYKACZEWSKI, K., PAXSON, A. T., ANAND, S., CHEN, X., WANG, Z. & VARANASI, K. K. 2012*b* Multimode multidrop serial coalescence effects during condensation on hierarchical superhydrophobic surfaces. *Langmuir* **29**, 881–891.

SPRITTLES, J. E. & SHIKHMURZAEV, Y. D. 2012 Coalescence of liquid drops: different models versus experiment. *Phys. Fluids* **24**, 122105.

THORODDSEN, S. T., TAKEHARA, K. & ETOH, T. G. 2005 The coalescence speed of a pendent and a sessile drop. *J. Fluid Mech.* **527**, 85–114.

TRINH, E. & WANG, T. G. 1982 Large-amplitude free and driven drop-shape oscillations: experimental observations. *J. Fluid Mech.* **122**, 315–338.

TSAI, P., HENDRIX, M. H. W., DIJKSTRA, R. R. M., SHUI, L. & LOHSE, D. 2011 Microscopic structure influencing macroscopic splash at high weber number. *Soft Matt.* **7**, 11325–11333.

WANG, F. C., YANG, F. & ZHAO, Y. P. 2011 Size effect on the coalescence-induced self-propelled droplet. *Appl. Phys. Lett.* **98**, 053112.

WATSON, J. A., CRIBB, B. W., HU, H. M. & WATSON, G. S. 2011 A dual layer hair array of the brown lacewing: repelling water at different length scales. *Biophys. J.* **100**, 1149–1155.

WISDOM, K. M., WATSON, J. A., QU, X., LIU, F., WATSON, G. S. & CHEN, C. H. 2013 Self-cleaning of superhydrophobic surfaces by self-propelled jumping condensate. *Proc. Natl Acad. Sci. USA* **110**, 7992–7997.

YUE, P., FENG, J. J., LIU, C. & SHEN, J. 2004 A diffuse-interface method for simulating two-phase flows of complex fluids. *J. Fluid Mech.* **515**, 293–317.

YUE, P., ZHOU, C. & FENG, J. J. 2006*a* A computational study of the coalescence between a drop and an interface in Newtonian and viscoelastic fluids. *Phys. Fluids* **18**, 102102.

YUE, P., ZHOU, C. & FENG, J. J. 2007 Spontaneous shrinkage of drops and mass conservation in phase-field simulations. *J. Comput. Phys.* **223**, 1–9.

YUE, P., ZHOU, C., FENG, J. J., OLLIVIER-GOOCH, C. F. & HU, H. H. 2006*b* Phase-field simulations of interfacial dynamics in viscoelastic fluids using finite elements with adaptive meshing. *J. Comput. Phys.* **219**, 47–67.

ZHANG, Q., HE, M., CHEN, J., WANG, J., SONG, Y. & JIANG, L. 2013 Anti-icing surfaces based on enhanced self-propelled jumping of condensed water microdroplets. *Chem. Commun.* **49**, 4516–4518.

ZHOU, C., YUE, P., FENG, J. J., OLLIVIER-GOOCH, C. F. & HU, H. H. 2010 3D phase-field simulations of interfacial dynamics in Newtonian and viscoelastic fluids. *J. Comput. Phys.* **229**, 498–511.